Journal of the European Ceramic Society 44 (2024) 7490–7503

Contents lists available at ScienceDirect

Journal of the European Ceramic Society

journal homepage: www.elsevier.com/locate/jeurceramsoc

# A macroscale damage model for the tensile and bending failure of C/C-SiC structural laminates

Edoardo Novembre [a,*], Alessandro Airoldi [a], Marco Riva [a], Antonio Maria Caporale [a], Lorenzo Cavalli [b], Mario De Stefano Fumo [c]

[a] Dept. of Aerospace Science and Technology, Politecnico di Milano, Via La Masa 34, Milano 20156, Italy
[b] Petroceramics SpA, Viale Europa, Stezzano (BG) 24040, Italy
[c] Italian Aerospace Research Centre, CIRA, Via Maiorise, Capua (CE) 81043, Italy

ARTICLE INFO

*Keywords:*
Ceramic matrix composites
Finite element analysis
Continuum damage mechanics
Non-linear response
Strength

ABSTRACT

This work presents a Finite Element approach to model the in-plane mechanical behavior of C/C-SiC fabrics at the lamina level, including the non-linear response of diverse lay-ups and the bending-to-tensile strength ratio at failure. The material model employs a decomposition into two idealized phases, which can be exploited to capture matrix- and fiber-dominated responses at a high level of abstraction. The constitutive law of the matrix phase adopts a Continuum Damage approach driven by two Tsai-Wu surfaces, while a quasi-brittle behavior is attributed to the fibers phase. This decomposition effectively represents the influence of matrix degradation on the response and failure of the laminates. Moreover, simulations reveal that a statistical distribution of the strength is required to represent some of the experimental outcomes. The correlation with experimental data that was achieved points out that the technique is a promising tool for supporting the early design phase of CMC structures.

## 1. Introduction

Ceramic Matrix Composites are a class of advanced materials that combine superior operational temperatures together with significant structural capabilities. In general, CMCs consist in a refractory ceramic matrix toughened by long fibers, short fibers or particles that provide the material remarkable thermal stability. In the last two decades, an increasing attention arose around this class of materials because of their potential application as lightweight Thermal Protection Systems (TPS) and Hot Structures for reusable space vehicles and hypersonic vehicles [1–3].

CMCs offer an almost unique combination of mechanical, thermal and tribological properties, largely due to the toughening mechanisms that occur at the interphase between matrix and reinforcement. The result is a significant compensation of the inherent brittleness of the bulk ceramic, and increased damage tolerance and reliability [4]. Among the available ceramic matrices, Silicon Carbide (SiC) stands out for its low density, significant thermal stability, and superior strength at elevated temperatures [5–7].

SiC matrix reinforced with long carbon fibers is commonly referred to as C/SiC. This specific family of composites gained particular interest as its manufacturing cost greatly decreased after the introduction of Liquid Silicon Infiltration (LSI), an innovative manufacturing technique developed in the DLR research center of Stuttgart, Germany [8]. This technique consists in the infiltration of molten liquid silicon inside a soft porous carbonaceous char, which is obtained from the pyrolysis of a carbon-phenolic (CPC) preform. Part of the infiltrated silicon reacts with char preform forming SiC, while the remaining forms an amorphous silicon phase. Where silicon is not able to infiltrate the char, the material retains a certain amount of porosity. Moreover, infiltrated silicon tends to react with carbon fibers, degrading their properties [9]. Studies on the kinetics of the infiltration process showed that different phases of SiC and Si form with different dimensions, ranging from the nano- to the micro-scale [10–12]. Considering this morphological heterogeneity and the high temperatures reached during the manufacturing process, the cooling phase leads to Thermal Residual Stresses (TRSs) inside the material and a network of fine cracks [6,9]. C/SiC has already found technological and industrial applications as hot structure [13], in brake systems [6], and in ballistic armors [14].

In this work, the in-plane mechanical properties of a C/C-SiC

* Corresponding author.
*E-mail address:* edoardo.novembre@polimi.it (E. Novembre).

https://doi.org/10.1016/j.jeurceramsoc.2024.05.072
Received 16 January 2024; Received in revised form 18 April 2024; Accepted 29 May 2024
Available online 31 May 2024

composite with a twill weave 2/2 fabric reinforcement are investigated both from an experimental and numerical point of view. The objective of the activity is that of formulating an effective numerical constitutive law that, within the typical damage tolerant approach of the aerospace field, can support the early design phase of reusable hot structures. This task poses several challenges, as predicting the response of CMCs requires the development of complex material laws to account for the non-linear behavior typical of this class of materials, as illustrated in several literature works that addressed the modelling of non-linear response and failure in CMC laminates [15–19].

Among the approaches presented in literature for CMCs, the numerical modelling of LSI-C/SiC has been addressed by Hofmann et al. in [20,21]. In [20] a significant bending to tensile strength ratio was experimentally identified and numerically investigated, and in [21] FE models were produced to predict the response of the material in the presence of interlaminar defects. The non-linear behavior of the material was adequately represented by using an elastic plastic model based on generalized anisotropic Hill yield criterion and failures were introduced by embedding Cohesive Elements in predefined regions of the Finite Element models. The toughness attributed to the Cohesive Zone Models (CZM) was exploited to capture the bending to tensile ratio, which was represented with underestimation between 8 % and 17 %. An approach based on CZM was adopted also in [22] to simulate Double Cantilever Beam tests.

Another viable solution to model the in-plane matrix dominated response of CMCs is to rely on a binary decomposition of the material. Binary Models (BM) were originally formulated in [23–25] for the case of polymer matrix composites with 3D reinforcement, and then successfully assessed in [26,27] for CMCs. The key aspect of the BM is that the composite is decomposed in two constituents: reinforcing tows, represented by one-dimensional elements, and an effective medium, embodied in solid elements. The former accounts for the axial stiffness of the reinforcement, whereas the latter is attributed the remaining properties of the laminate and is mainly responsible for reproducing the matrix-dominated response of the laminate. The effective medium was assumed as isotropic in the elastic range. The same approach was slightly modified in [27], in which a plasticity model based on Drucker-Prager yield criterion was associated to the effective medium with the aim of representing the effects of progressive matrix damages. The material investigated in [27] was a SiC/SiC CMC with fibers in a 3D interlock woven structure. More recently, a CDM based BM was adopted in [28] to tackle two of the blind prediction challenges proposed within the Enhanced Physics-based Prognosis and Inspection of CMCs (EPPIC) program [29]. The overall tensile response of plain and drilled SiC/SiC specimens achieved with Abaqus was in good agreement with the validation data, even if the ultimate strain and the proportional limit stress were underestimated. One of the advantages of the BM approach is the capability to model progressive matrix degradation separately from fiber response.

In the work presented in this paper a material model that relies on a bi-phasic decomposition of the laminate was applied, in analogy with the BM presented in literature. Such a choice was made to propose an approach aimed at representing non-linear responses in tension and in bending, as well as the failure of the laminates, with a single constitutive law, taking into account the statistical distribution of properties and considering the need of capturing the bending to tensile strength ratio. Moreover, it will be shown that the bi-phasic decomposition enables the representation of the key role of damage in the matrix on the ultimate failure of the material in the direction of reinforcement fibers, a typical mechanism of CMCs that is well described in literature [30–32].

The approach was inspired by the method devised in [33], which focused on the numerical modelling of inter- and intra-laminar damage mechanisms in polymer matrix composites. The framework of the numerical technique presented in [33] allows to model the matrix-dominated in-plane inelastic processes, which this work addressed through a damage model based on the Tsai-Wu strength criterion, and the onset and development of delamination. Although delamination occurs in the LSI-C/C-SiC material considered in this study [34], such aspect is outside the scope of the present work. Additionally, the model does not include the representation of permanent residual strain, which can be reconducted to the thermal residual stress and friction in the material, as proposed in [30].

After this introduction, Section 1 presents the experiments that were performed and discusses the results. Tensile and bending tests were carried out on specimens with different layups to investigate the elastic properties as well as the strength and overall response of the laminates. In Section 2, the basic aspects of the numerical approach and the constitutive laws are illustrated, accompanied by the procedure that was used to identify all the parameters required by the damage model. Finally, the capabilities of the numerical model are illustrated and the correlation between experimental and numerical results is shown.

## 2. Experimental activities

### 2.1. Materials and method

The scope of the activity presented in this work is the development of a modelling technique capable of predicting the non-linear response and failure of C/C-SiC laminates when subjected to in-plane stress states. The characterization of the response of such laminates was carried out considering both tensile and bending tests at room temperature with a variety of lamination sequences, so to provide the basis for a calibration and a validation of the constitutive model.

#### 2.1.1. Material under investigation

The material considered in the study is the C/C-SiC shown in Fig. 1, a continuous carbon fiber reinforced ceramic composite with a silicon carbide matrix. The material was manufactured through the LSI process. The green preform was obtained by means of the vacuum bag technology. Phenolic resin pre impregnated layers of 2/2 twill fabric were manually stacked on an aluminium mould. The preform was compacted in autoclave at a pressure below 1.2 MPa, at a maximum temperature of 180°C. The phenolic resin was selected as precursor due to its high carbon yield (55–60 mass%). This property provides a dimensionally stable structure that can be handled and optionally machined after the pyrolysis processes. The green sample was pyrolyzed in nitrogen flow at a maximum temperature of 950°C. During this heating treatment the polymer matrix was transformed to an amorphous and porous carbon matrix. This matrix is intimately micro cracked due to the dimensional shrinkage of the resin that occurs during the pyrolysis treatment. The porous carbon preform was subsequently densified with molten silicon in the liquid silicon infiltration process that was performed at a maximum temperature of 1650°C at a vacuum level below 100 Pa. During this process the silicon entered the preform by capillarity and reacted with the carbon, thus forming silicon carbide. After the infiltration process a little amount of free silicon (3–5 mass%) was still present in the composite matrix due to the incomplete reaction with the

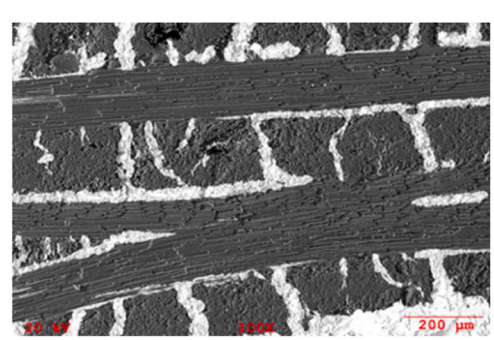


**Fig. 1.** Microstructure of the C/C-SiC under investigation.

carbon preform.

### 2.1.2. Tensile and bending tests

Tensile tests were performed on specimens with four different layups: "*T0*" ($[0]_{20}$ layup), "*T45*" ($[45/-45]_{10s}$ layup), "*T30*" ($[30/-30]_{10s}$ layup), and "*TQI*" or "*quasi-isotropic*" ($[0/45/90/-45]_{5s}$ layup). The standard ASTM C1275–15 [35] was taken as a guideline to design the specimens and perform the tests, which for this class of materials may require specific and tight precautions [36]. All the specimens were dog-bone shaped, with a total length of 200*mm*, a gauge length of 45*mm*, and an average thickness of $4.21 \pm 0.08$*mm*. The width of the broad part of the specimen was 10*mm* and the average gauge width was of $7.98 \pm 0.02$*mm*. The geometry of the specimen is sketched in Fig. 2(a). Four fiberglass-reinforced tabs were applied at the extremities of every specimen where they were gripped by the testing machine. In this way, the load applied by the clamps was progressively distributed in the specimen, avoiding undesired stress concentration in the clamping area. Tabs were made using a fabric glass-reinforced composite with epoxy matrix and were 77 mm long along specimen axis and 2.4 mm thick. A lamination sequence $[45]_{12}$ was adopted. A tapering of $14° \pm 1°$ was obtained on every tab by machining. Tabs were applied to the specimens by using a film of Scotch Weld AFK 163–2 K, an epoxy-based structural adhesive. Specimens were equipped with a biaxial strain gauge and an extensometer. An MTS 810 Material Testing System was used together with an acquisition system that sampled the crosshead displacement, the applied force and the signals coming from the extensometer and the strain gauge at a frequency of 10*Hz*. The tests were performed imposing a displacement velocity of 0.5 *mm*/min. Loading/unloading cycles were carried out to evaluate the presence of residual deformation.

Regarding the flexural tests, three-point bending was performed taking ASTM C1341–13 [37] as a guideline, on specimens with two different layups: "*B0*" with lamination sequence of $[0]_{20}$ and "*BQI*" or "*quasi-isotropic*" with a lay-up of $[0/45/90/-45]_{5s}$. As suggested by ASTM C1341–13 standard, three-point bending tests with a span-to-depth ratio of 32:1 were adopted to evaluate in-plane bending properties of the material avoiding undesired transverse shear effects. All the specimens had a length of 145*mm*, an average thickness of $4.09 \pm 0.03$*mm*, and an average width of $12.14 \pm 0.11$*mm*. The tests were performed on a MTS 858 material testing machine acquiring displacement and force with an acquisition frequency of 15*Hz*, at an imposed displacement rate of 0.5 *mm*/min. Moreover, in some of the tests strain gauges were placed on opposite sides with respect to the thickness and approximatively in the midpoint between one of the two supports and the loading nose. Three steel cylinders with a diameter of 15*mm* were adopted as load application nose and supports, as shown in the lay-out reported in Fig. 2(b). The span between the two external cylinders was of 128*mm*. Finally, also in this case loading/unloading cycles were performed to evaluate the eventual presence of residual deformation.

## 2.2. Experimental results and discussion

### 2.2.1. Results of tensile tests

The tensile tests were performed on five *T0* specimens, seven *T45*, five *T30*, and six *TQI* specimens. The set of responses obtained for each one of the four different families of specimens showed good repeatability between the different samples and each family exhibited a well-defined specific response. In Fig. 3(a), one representative curve for each family of specimen is reported. The responses obtained for all the *T45* specimens are reported in Fig. 3(b), to exemplify the scattering obtained within a family of specimens. All the engineering stress vs. strain curves were elaborated from load cell and the strain data acquired through an extensometer with a gauge length of 20 mm, which is considered suitable given that the measured unit cell size of the 2×2 twill fabric, as defined in [38], was approximately 8 mm.

It can be observed that every layup showed a certain amount of nonlinearity shortly after the start of the test, with an almost negligible linear elastic part of the response. Moreover, each curve showed some residual deformations and a loss of apparent elastic modulus. All these phenomena increased in magnitude as the angle between the fibers and the load application direction increased, thus indicating a matrix-dominated type of non-linearity. Failures happened in a sudden way with the total loss of the load bearing capability. The properties evaluated are reported in Table 1. As suggested by the standard [37], the stiffness value was obtained by computing the slope of the tangent of the curve between 0 $\mu\varepsilon$ and 200 $\mu\varepsilon$, where the response was deemed almost linear. The Poisson's ratio reported was obtained by the biaxial strain gages applied to the specimen. The value represents an estimate since the grid size is close to the unit cell size of the fabric and is equal to the specimen width. Accordingly, it cannot be guaranteed that such a value is representative of the homogenized material properties.

The non-linearity observed in the tests was already observed in literature [20,30] and was associated with the progressive degradation of the matrix, due to the evolution of the crack network that

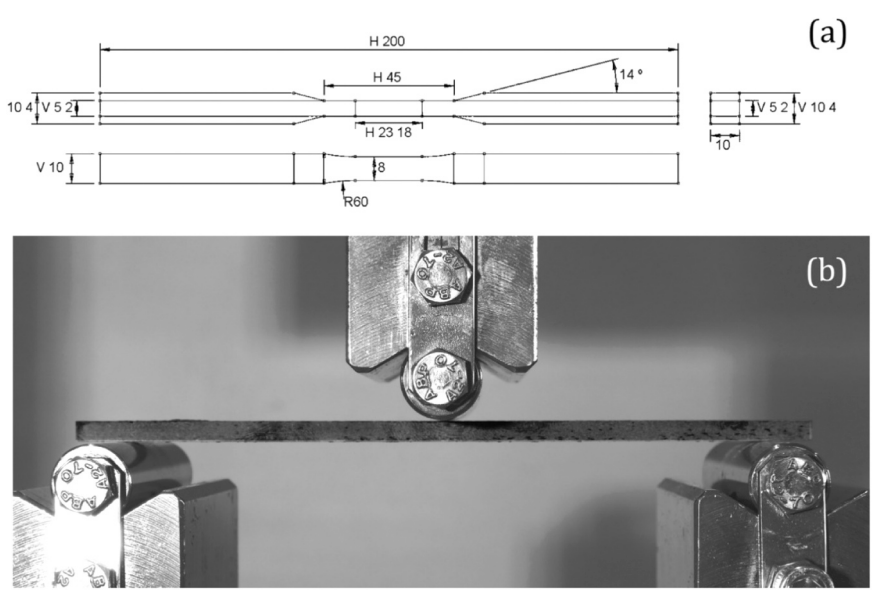


**Fig. 2.** (a) Geometry of a dogbone tensile specimen with tabs. (b) Example of configuration used in bending test.

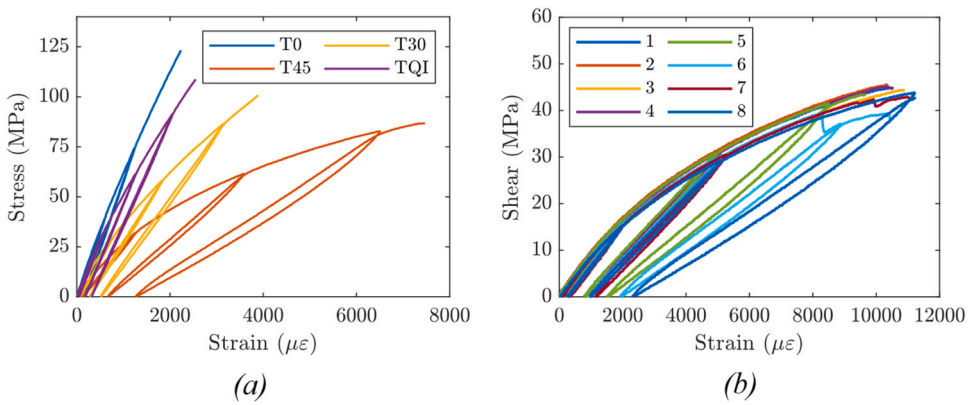


**Fig. 3.** (a) Representative experimental stress-strain response for the tensile tests with different lay-up. (b) Shear stress strain response of different specimens of batch T45.

**Table 1**
Properties evaluated after tensile tests.

| Specimen | Elastic modulus (GPa) | Failure Strength (MPa) | Failure Strain (με) | Poisson's Ratio |
|---|---|---|---|---|
| T0 | 74.1 ± 2.2 | 122.3 ± 8.9 | 2288 ± 202 | 0.020 ± 0.016 |
| T30 | 44.6 ± 5.0 | 106.7 ± 6.2 | 3844 ± 230 | 0.355 ± 0.033 |
| T45 | 31.8 ± 2.7 | 87.7 ± 2.3 | 8054 ± 765 | 0.548 ± 0.038 |
| TQI | 58.8 ± 2.2 | 108.0 ± 4.2 | 2542 ± 323 | 0.154 ± 0.018 |

characterizes the material. This damage mechanism led to a reduction of the elastic modulus of the material, which was clearly visible in the unloading/reloading cycles. As said previously, these phenomena were more relevant for matrix dominated lay-ups and primarily affected the *T45* and *T30* specimens. However, also for *T0* and *TQI* they could not be neglected, suggesting that the role of the matrix and of matrix-fiber interactions can significantly affect the stiffness of the material even when the load is aligned with the reinforcement. The modulus reduction and the presence of residual deformation can be explained with the evolution of a crack network at the microscale, which dissipates energy through development and propagation of the cracks and through friction between opposing crack faces.

In several specimens fibers pull-out was observed, as shown in Fig. 4 (a), referred to a *T45* specimen. This phenomenon is consistent with a failure characterized by the development of damage in the ceramic matrix opposed by a toughening effect originated by the presence of the fibers [30,31,39]. It is also worth noting that the material produced by LSI is characterized by the presence of defects both in the SiC matrix and inside the transverse sections of the fiber yarns, characterized by the presence of unreacted char, as it is visible in Fig. 1. The presence of such defects and the thermal residual stresses originated during the manufacturing process explain the early development of damage accumulation in the matrix and relative slip between the fiber yarns and the matrix.

The plies of *T45* shows fractures oriented at +/-45°, probably originated by the in-plane shear stress in the material, which tend to develop in a relatively large zone of diffused damage, as shown in the picture of the top view of a failed specimen reported in Fig. 4(b). The failure of *T0* and *T30* are neater, with fracture lines inclined at 90° and approximately at 60° with respect to the longitudinal axis respectively, as shown in Fig. 5. Finally, specimens *TQI* showed a hybrid fracture morphology, combining the failure mode of *T0* and *T45*, with a quite neat crack if inspected from the top view, as visible in Fig. 5.

### 2.2.2. Results of bending tests

The bending tests were performed on five *B0* and five *BQI* specimens using a three-point bending configuration, aiming at identifying the

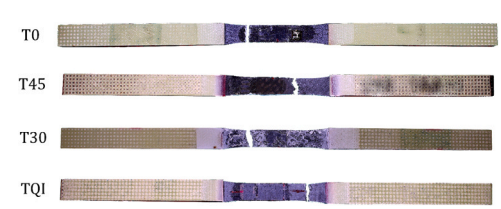


**Fig. 5.** Samples of T0, T45, T30, and TQI specimens after the tensile test.

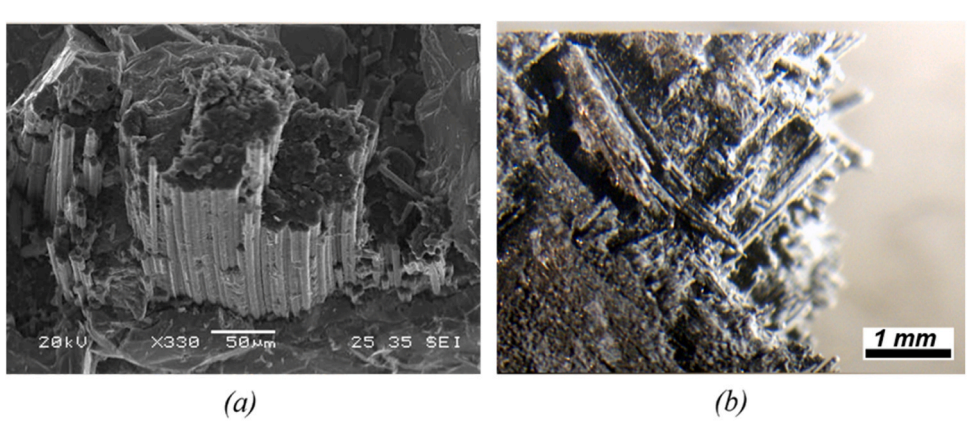


**Fig. 4.** Pull out in a T45 specimen (a) and top view of a tested T45 specimen (b).

flexural properties of the material. A representative stress-strain response for each set of specimens is reported in Fig. 6(a). These curves were elaborated using the Euler beam theory framework, as suggested by the standard [37]. Both sets of specimens showed a good repeatability in terms of qualitative response, even though the elastic modulus, the strength, and the ultimate strain between the different samples exhibited a non-negligible scattering, as reported in Table 2. The responses are more linear with respect to the tensile tests performed on the same types of lay-ups. It can be noticed also that the elastic modulus recorded during bending tests was lower than the one measured in tensile tests. Moreover, the outer layers of the laminates in bending tests reached a significantly higher strain and stress level. The possible motivation for these phenomena resides in the capability of the internal plies to provide some of the load carrying capability lost by the external ones and in the nature of the material, which presents statistically distributed properties. The statistical distribution led to higher flexural strength because, given the high stress gradient in the through-the-thickness direction during three-point bending, the volume of material subjected to the maximum stress level was significantly lower than in the tensile tests. The distribution of flaws in fibers was indicated as a possible cause for the bending to tensile strength ratio of CMCs also in [40,41].

The data recorded with the strain gauges placed on opposite faces highlighted that the neutral axis was located closer to the compressed face, as the tensile strain was about 1.15 times larger than the compressive one. Moreover, during the flexural test, the neutral axis slightly moved further in the direction of the compressed region, suggesting a progressive damaging occurring in the tensed plies.

Fig. 6(b) illustrates the final failure, which is a neat fracture line that during the three-point bending tests originated in the tensed side of the specimens. The fracture line passes through the yarns that are perpendicular to the longitudinal axis of the specimen, whereas many yarns parallel to the specimen axis bridge the matrix crack. Such morphology further supports the hypothesis of relative slip between fiber and matrix and is a clear indication that the final failure is triggered by the progressive accumulation of cracks in the material surrounding the fibers. This was also discussed in [30,31,36], where it was indicated that the fractures that can be observed in bending initially develop in the matrix, and that fibers are eventually broken because of stress concentrations induced by matrix damaging.

## 3. Development of a modelling technique

### 3.1. Outline of the numerical approach

This work aims at developing a material model capable of reproducing the key aspects of the response illustrated in the previous section. The requirements for the model can be summarized as: (a) capturing, in monotonic loading, the non-linear phenomena recorded for the different lay-ups; (b) predicting the maximum strength obtained in the tests, including the bending-to-tensile strength ratio; (c) accounting for the critical accumulation of damage in the matrix, which anticipates and contributes to the failure of the composite material. The last point, i.e. the specific role played by the ceramic matrix in the overall response of the composite material, represents a strong motivation for the adoption of a binary approach, based on the definition of two idealized fibers and the matrix phases.

**Table 2**
Properties evaluated after bending tests.

| Specimen | Elastic modulus (GPa) | Failure Strength (MPa) | Failure Strain (με) |
|---|---|---|---|
| B0 | 55.8 ± 7.9 | 175.3 ± 13.8 | 3034.9 ± 191.7 |
| BQI | 53.2 ± 9.0 | 182.0 ± 8.2 | 3438.5 ± 170.5 |

From the practical standpoint, the material model is intended to simulate structural elements, assist the design of CMC hot-structures and investigate critical structural features. Against this background, the numerical technique is formulated at a higher level of abstraction with respect to more refined micro-mechanical models, so that the macroscopical response of the laminate is simulated by idealizing both the material constituents and the damage mechanisms that occur at the microscale. A dedicated Continuum Damage Mechanics (CDM) approach embedded in FE models with one layer of elements per ply is adopted, using as a general framework the technique proposed in [33, 42].

#### 3.1.1. Biphasic decomposition of the composite

The basic concept behind the biphasic decomposition that was presented in [33] is a 3D generalization of the approach proposed in [43, 44] and it is consistent with the assumptions of the binary model developed and adopted in [23–27]. In such approaches, the idealized matrix phase is an effective medium that represents the non-linear matrix-dominated responses of the laminate, whereas the idealized fiber phase accounts for the effects of the continuity of the reinforcing fibers. Accordingly, the idealized fibers phase in the CMC model presented in this paper was characterized only by stiffness terms in the reinforcement direction, and the remaining properties of the laminate were assigned to the matrix idealized phase. Continuum Damage Mechanics was applied to model matrix damage accumulation as well as the final pull-out and breakage of the fibers, by attributing different damage parameters to the separated phases. It must be remarked that the model does not constitute a micromechanical approach, since these idealized phases are superimposed and defined in the same volume, so that they obey to constitutive laws that are formulated as a function of the same averaged strain at the homogenized ply level. In the case of a woven composite, these considerations lead to the elastic response expressed in Eq. 1, where the $6 \times 6$ matrices are the stiffness matrices of the fiber and of the matrix phase, 1 and 2 are the reinforcement directions in the fabric ply and 3 is the direction normal to the laminate. Continuum Damage Mechanics was applied within this frame to

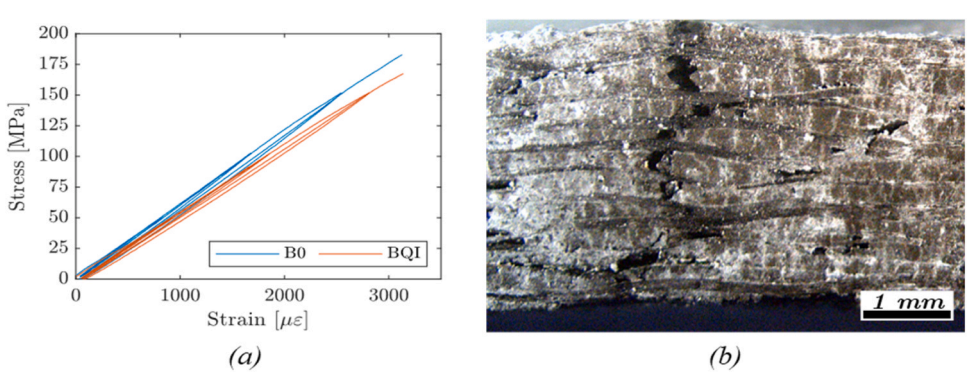


**Fig. 6.** (a) Bending stress strain curve. (b) Bridging effect on a B0 specimen.

separately degrade the two phases.

$$\begin{bmatrix} \sigma_{11} \\ \sigma_{22} \\ \sigma_{33} \\ \tau_{12} \\ \tau_{23} \\ \tau_{31} \end{bmatrix} = \left( \begin{bmatrix} D^f_{11} & 0 & 0 & 0 & 0 & 0 \\ 0 & D^f_{22} & 0 & 0 & 0 & 0 \\ 0 & 0 & 0 & 0 & 0 & 0 \\ 0 & 0 & 0 & 0 & 0 & 0 \\ 0 & 0 & 0 & 0 & 0 & 0 \\ 0 & 0 & 0 & 0 & 0 & 0 \end{bmatrix} + \begin{bmatrix} D^m_{11} & D^m_{12} & D^m_{13} & 0 & 0 & 0 \\ D^m_{21} & D^m_{22} & D^m_{23} & 0 & 0 & 0 \\ D^m_{31} & D^m_{32} & D^m_{33} & 0 & 0 & 0 \\ 0 & 0 & 0 & D^m_{44} & 0 & 0 \\ 0 & 0 & 0 & 0 & D^m_{55} & 0 \\ 0 & 0 & 0 & 0 & 0 & D^m_{66} \end{bmatrix} \right) \begin{bmatrix} \varepsilon_{11} \\ \varepsilon_{22} \\ \varepsilon_{33} \\ \gamma_{12} \\ \gamma_{23} \\ \gamma_{31} \end{bmatrix} \tag{1}$$

The main issue associated to the decomposition procedure was the development of an algorithm that, at the same time, could obtain a physically admissible stiffness matrix for the idealized matrix phase and a reasonable approximation of the effective stiffness contribution of the fibers in the reinforcement direction [43]. In the binary model adopted in [27] the matrix material was identified though a trial-and-error procedure, while in [33] the three-dimensional decomposition was achieved through an analytical algorithm based on the control of the Poisson's ratios of the idealized matrix phase.

In the present case, the decomposition algorithm was driven by the data provided in Table 3, where superscript $c$ refers to the properties of the whole composite prior to decomposition. Due to the fabric architecture of the reinforcement, the only matrix-dominated stiffness property that was possible to extrapolate from experiments was the in-plane shear modulus $G^c_{12}$ . The out-plane shear moduli, $G^c_{13}$ and $G^c_{23}$, were set equal to $G^c_{12}$. Despite not supported by experimental data, this choice was made for practical reasons. Finally, the out-of-plane modulus, $E^c_{33}$, was set equal to about $2G_{ij}$ and the out-of-plane Poisson's ratios were set to 0.3.

Then a 3D decomposition was carried out by considering an effective stiffness for the fiber, namely $E^f = 200GPa$, which could represent a reasonable value for the contribution of the fiber phase to the composite stiffness, also considering the degradation induced by the Silicon infiltration. The stiffness contribution of the reinforcement to the composite was related to the stiffness terms $E^f$ as in Eq. 2, where $V^f_1$ and $V^f_2$ are the volumetric fractions in the two principal direction of the fabric. In the present application $V^f_1 = V^f_2 = 0.25$, for a total volumetric fraction of 0.5.

$$\begin{aligned} D^f_{11} &= V^f_1 E^f \\ D^f_{22} &= V^f_2 E^f \end{aligned} \tag{2}$$

The decomposition algorithm moved from the stiffness matrix of the whole composite, considering that the assumed value for $E^f$ led by subtraction to the stiffness matrix of the matrix phase (see Eq. 1). From the knowledge of such 6×6 matrix, the engineering constants of the idealized material constituting the matrix phase were checked by inverting the standard expressions for the stiffness matrix of an orthotropic material as a function of its engineering constants [45]. The results of this procedure, reported in Table 4, indicate that the value $E^m_{11} = E^m_{22}$ obtained are close to assumed value of $E^c_{33}$, so that the decomposition is in acceptable accordance with the assumption of isotropic matrix phase, which was introduced in the BM approaches proposed in [23,24]. Within the FE model the two phases are embedded in distinct 8-noded hexahedral elements with shared nodes so that, as already mentioned, they are subjected to the same strain at the ply level (see Eq. 1).

### 3.1.2. Tsai-Wu function for in-plane matrix damaging

The Tsai-Wu strength criterion [46] is suited for anisotropic materials with different behavior in tensile or compressive stress state and it has already been applied in different shapes and with various purposes to the modelling of CMCs [47–49]. Considering a failure originated by in-plane stress state in an orthotropic material, the Tsai-Wu failure surface can be expressed in the material principal axes as in Eq. 3 [50].

$$F_1\sigma_1 + F_2\sigma_2 + F_{11}\sigma_1^2 + F_{22}\sigma_2^2 + 2F_{12}\sigma_1\sigma_2 + F_{66}\tau_{12}^2 = 1 \tag{3}$$

Most of the coefficients that define Eq. 3 can be easily related to the strengths of the material along its principal axes, as shown in Eq. 4. The strengths of the material are indicated as $S^{T,C}_{ij}$, where subscripts refer to the direction in material axis and the superscript refers to tensile ($T$) or compressive ($C$) stress state.

$$\begin{cases} F_i = \dfrac{1}{S^T_{ii}} - \dfrac{1}{S^C_{ii}} \quad F_{ii} = \dfrac{1}{S^T_{ii}S^C_{ii}} \quad i = 1,2 \\ F_{66} = \dfrac{1}{S^2_{12}} \end{cases} \tag{4}$$

On the contrary, there are not standard methods to determine the interaction parameter $F_{12}$, which would require testing the material in a biaxial stress state that is extremely difficult to obtain in experiments. However, if a closed failure envelope is required, $F_{12}$ can be bound inside specific ranges [46], even if recent studies suggest that an open envelope should not be discarded a priori [50]. In this work, the Tsai-Wu function was used to define the damage threshold and the damage evolution laws for the idealized matrix phase.

The remarkable non-linearities observed during experiments were attributed to the progressive accumulation of damage inside the complex structure of the ceramic matrix surrounding the yarns and of the char residuals inside the yarns. In the proposed approach, this phenomenon is represented by the degradation of the in-plane elastic properties of the idealized matrix phase through a single scalar damage variable $d_m$. As a consequence, the development of permanent deformation at unloading is not modelled. This choice does not affect the possibility to adequately evaluate the state of stress and to predict the failure of the laminates in monotonic load conditions. Following a Continuum Damage Mechanics approach, the damaged compliance matrix for the matrix phase is written as in Eq. 5.

**Table 3**
Composite properties before the biphasic decomposition.

| Elastic properties | Value |
|---|---|
| $E^c_{11} = E^c_{22}$ | 73.6 $GPa$ |
| $E^c_{33}$ | 20.0 $GPa$ |
| $G^c_{12} = G^c_{13} = G^c_{23}$ | 11.2 $GPa$ |
| $\nu^c_{12}$ | 0.01 |
| $\nu^c_{13} = \nu^c_{23}$ | 0.3 |

**Table 4**
Idealized phases properties.

| Elastic properties | Value |
|---|---|
| $E^m_{11} = E^m_{22}$ | 23.6 $GPa$ |
| $E^m_{33}$ | 18.1 $GPa$ |
| $G^m_{12} = G^m_{13} = G^m_{23}$ | 11.2 $GPa$ |
| $\nu^m_{12}$ | 0.0312 |
| $V^f_1 = V^f_2$ | 0.25 |
| $E^f$ | 200.0 $GPa$ |

$$\begin{bmatrix} \varepsilon_{11}^m \\ \varepsilon_{22}^m \\ \gamma_{12}^m \end{bmatrix} = \begin{pmatrix} \frac{1}{(1-d_m)E_{11}^m} & \frac{\nu_{21}^m}{E_{22}^m} & 0 \\ \frac{\nu_{12}^m}{E_{11}^m} & \frac{1}{(1-d_m)E_{22}^m} & 0 \\ 0 & 0 & \frac{1}{(1-d_m)G_{12}^m} \end{pmatrix} \begin{bmatrix} \sigma_{11}^m \\ \sigma_{22}^m \\ \tau_{12}^m \end{bmatrix} \tag{5}$$

The possibility of capturing the non-linearities exhibited in the tests with such a simplified approach relies on the separation of matrix-dominated responses from the fiber-dominated ones, which is intrinsic to the bi-phasic approach.

The damage evolution is driven by the in-plane stress state in the matrix phase by using functions shaped as the square root of Eq. 3, i.e. as the square root of the value of the in-plane Tsai-Wu criterion. Within a Damage Mechanics Approach, this function is formulated in terms of the effective stresses $\tilde{\sigma}_{ij}^m$, that are computed as a function of the actual stress components in the matrix phase as in Eq. 6.

$$\tilde{\sigma}_{11}^m = \frac{\sigma_{11}^m}{1-d_m} \quad \tilde{\sigma}_{22}^m = \frac{\sigma_{22}^m}{1-d_m} \quad \tilde{\tau}_{12}^m = \frac{\tau_{12}^m}{1-d_m} \tag{6}$$

Hence, the damage onset function reads as Eq. 7.

$$f(\tilde{\sigma}^m) = \sqrt{F_1\tilde{\sigma}_{11}^m + F_2\tilde{\sigma}_{22}^m + F_{11}(\tilde{\sigma}_{11}^m)^2 + F_{22}(\tilde{\sigma}_{22}^m)^2 + 2F_{12}\tilde{\sigma}_{11}^m\tilde{\sigma}_{22}^m + F_{66}(\tilde{\tau}_{12}^m)^2} \tag{7}$$

The threshold for damage onset corresponds to the locus of the effective stress components where Eq. 8 holds:

$$f(\tilde{\sigma}^m) = 1 \tag{8}$$

Accordingly, the $F_i$ and $F_{ij}$ parameters in Eq. 7 can be calibrated by choosing $S_{ij}^{T,C}$ as the proper stress components that act in the matrix idealized phase when the deviation from linearity occurs.

### 3.1.3. Damage evolution law for the matrix

After the onset, the evolution of the in-plane damage variable in the matrix phase is dictated by the law written in Equation 9: a piecewise function that depends on the value of $f(\tilde{\sigma}^m)$ and on some shape parameters ($a_i$, $b_i$ and $c_i$), for $i = 1, 2$. The transition from the first expression to the second one occurs at a given value $f_1$ of the function $f(\tilde{\sigma}^m)$, as indicated in Equation 9. Finally, $f_2$ bounds the interval of validity for the piecewise function.

$$d_m(f(\tilde{\sigma}^m)) = \begin{cases} 0 & \text{if } f < 1 \\ c_1 + a_1 f + \frac{b_1}{f} & \text{if } 1 \le f < f_1 \\ c_2 + a_2 f + \frac{b_2}{f} & \text{if } f_1 < f < f_2 \end{cases} \tag{9}$$

The shape of the evolution law was specifically selected for an accurate representation of the strain hardening part of the non-linear response. The evolution law of the single damage parameter was calibrated by considering the response of the *T45* test and by adopting the algorithm presented in subsection 2.2.1. Thereafter, the damage threshold criterion expressed in Eq. 8 and the damage evolution law represented in Equation 9 were assessed in the simulation of other layups, where they provided a very good correlation with the experimental non-linear curves, as it will be clearly shown in Section 2.2 and it is represented, for instance, in Fig. 7.

The final step for the calibration of matrix damage law was the introduction of a strain softening regime in the matrix phase, so that the neat fractures that were observed in the physical ceramic matrix during the experiments could be accounted for in the models through a steep decrease of load bearing capability and a consequent strain localization in the FE models of the coupons.

After some attempts, it was evidenced that the shape of $f(\tilde{\sigma}^m)$ was not adequate to correctly represent both the progressive accumulation of damage in the matrix (threshold and evolution) and the limit for the triggering of the strain softening regime, required to model failure events. The plot in Fig. 7 exemplifies a case were the non-linear response was captured, but failure could not be represented with the same calibration based on *T45* test. Accordingly, a new function was introduced, referred to as $f^u(\tilde{\sigma}^m)$, which was still formulated as the square root of an in-plane Tsai-Wu surface, but with different coefficients $F_i$ and $F_{ij}$. Such a function was only introduced to define the limit of validity of the damage evolution equations reported in Equation 9. Hence, when the stress state is such that $f^u$ reaches a given value $f_1^u$, the damage is evaluated still as a function of $f(\tilde{\sigma}^m)$, but according to the new evolution law described in Eq. 10. The value $f_1^u$ that triggers the strain softening must be reached by $f^u(\tilde{\sigma}^m)$ before $f(\tilde{\sigma}^m)$ reaches its validity limit $f_2$.

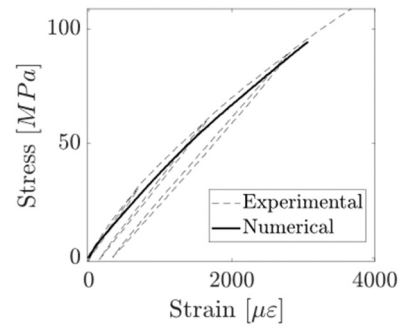


**Fig. 7.** Non-linear response of a T30 specimen after the calibration of matrix damage law.

$$d_m = 1 - \left(1 - d_m^l\right)\left(\frac{f^l}{f}\right)^p \quad \text{if } f^u \ge f_1^u \tag{10}$$

The values $d_m^l$ and $f^l$ in Eq. 10 refer to the last values assumed by the damage and by the function $f(\tilde{\sigma}^m)$ before the condition $f^u \ge f_1^u$ is met. This guarantees the continuity of the damage evolution when strain softening is activated. Moreover, a non-healing condition was implemented to assure that, for any given stress state, damage could not decrease nor become negative. The parameter $p$ is used to regulate the decay of stress with the growing strain in the matrix phase and defines the shape of the stress vs. strain curve of the matrix in the strain softening regime, which means that the calibration of $p$ depends on the mesh size, and changing the mesh refinement of the model would require adapting this strain softening parameter. The evolution of the matrix damage as a function of $f(\tilde{\sigma}^m)$ and the effect of the exponent $p$ on strain softening is qualitatively represented in Fig. 8.

### 3.1.4. Damage model for fibers failure

A quasi-brittle response was attributed to the idealized fibers phase, which was regulated by a simple bilinear law including two scalar damage variables that degrade the load carrying capability of the reinforcement phase in the two directions. Also in this case, a non-healing

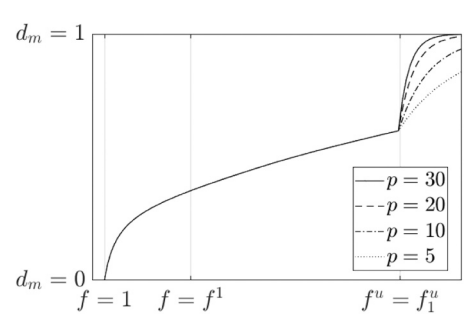


**Fig. 8.** Evolution of $d_m$ with different values of $p$.

condition was included. Considering the in-plane directions 1 and 2, the response was formulated as a function of the effective stress components $\tilde{\sigma}^f_{ii}$ in the fibers phase, defined in Equation 11. The evolution of the damage variables $d^f_i$ is reported in Eq. 12, where $m$ is a fixed parameter. The intervals of the piecewise function that defines $d^f_i$ are marked by two threshold values for the effective stress: a damage initiation stress ($\sigma^f_{di}$) and a failure stress at which the load carrying capability of fibers became null ($\sigma^f_{df}$). Damage in the fibers phase can be triggered and can evolve only in tensile stress state, and this means that $d^f_i$ is updated using Eq. 12 only when $\varepsilon^f_{ii} > 0$. The actual stress carried by the fibers phase is finally computed as written in Eq. 13.

$$\tilde{\sigma}^f_{ii} = E^f_{ii}\varepsilon^f_{ii}, i = 1,2 \quad (11)$$

$$d^f_i(\tilde{\sigma}^f_{ii}) = \begin{cases} 0 & if\ \tilde{\sigma}^f_{ii} < \sigma^f_{di} \\ m(\tilde{\sigma}^f_{ii} - \sigma^f_{di}) & if\ \sigma^f_{di} \le \tilde{\sigma}^f_{ii} \le \sigma^f_{df} \\ 1 & if\ \tilde{\sigma}^f_{ii} > \sigma^f_{df} \end{cases} \quad (12)$$

$$\sigma^f_{ii} = \tilde{\sigma}^f_{ii}\left(1 - d^f_i\right) \quad (13)$$

### 3.2. Numerical results and discussion

#### 3.2.1. Identification of the model parameters

The material law defined in the previous section required the calibration of different parameters, which was carried out by adopting different identification strategies depending on the parameter subjected to tuning. The first calibration step was dedicated to the identification of the parameters that regulates the damage onset and accumulation in the matrix idealized phase, which determine the non-linear part of the ply response before the failure.

For the Tsai-Wu shaped function $f(\tilde{\sigma}^m)$, it was chosen to set $F_{12}$ equal to zero, which entails that the failure surface is a closed ellipsoid. A sensitivity analysis was performed to identify the other coefficients, focusing on the deviation from the linear behavior exhibited in the tests with different lay-ups. This study resulted in the following outcome: $F_1 = F_2 = 0$, $F_{11} = F_{22} = 2.5\ 10^{-2}$ and $F_{66} = 7.216\ 10^{-2}$. Such choices determined the damage threshold, which is reached when $f(\tilde{\sigma}^m) = 1$.

To determine the evolution of the in-plane damage in the matrix phase, regulated by Equation 9, the calibration of parameters $a_1$, $b_1$, $c_1$, $a_2$, $b_2$, $c_2$ and $f_1$ was required. Since the tensile test with [±45] lamination sequence presented the most significant deviation from linearity, the calibration was carried out to match as close as possible this curve. After introducing some simplifying assumptions, the analytical algorithm reported in Appendix A1 was developed to obtain the evolution law parameters. The resulting values are reported in Table 5.

Regarding the strain-softening threshold function, it was required the tuning of an extensive set of parameters. This task was particularly demanding, since the strain-softening was the main driver of the failure of specimens with different lay-ups and a trial-and-error tuning would most likely be inadequate to calibrate a set of parameters suited for all the experimental tests. This motivated the implementation of the numerical identification strategy reported in Appendix A2, which was based on a Monte Carlo like method. The analyses were performed by using the Abaqus/Explicit solver and the constitutive laws of the idealized phases were implemented in a VUMAT subroutine. The matrix and the fibers idealized phases were attributed to C3D8R elements available in the Abaqus/Explicit library [51]. Models also comprised specimen tabs that were meshed with linear hexahedral elements (C3D8R) (see Fig. 9), and load was introduced in the specimen by applying a smoothly increasing velocity to the tabs gripped surfaces. The model comprised approximately 380k elements with characteristic dimension of $0.5 \times 0.5 \times 0.2\ mm$. The threshold parameter $f^u_1$ was statistically distributed in the volume of the material according to a normal distribution, since nothing suggested any other specific probability functions [52]. This choice was meant to represent the well-known defects and irregularities that are present in the ceramic matrix.

Fig. 10 illustrates the two calibrated Tsai-Wu surfaces in the effective stress planes $\sigma_{11} - \tau_{12}$ and $\sigma_{11} - \sigma_{22}$, considering $f^u = f^u_1$ and $f = f_1$. The light-blue band for the strain softening curve is a graphical representation of the statistic distribution of $f^U_1$, and its upper and lower bounds were determined by summing and subtracting the standard deviation to the mean value. The experimental campaign did not allow to calibrate the damage law of the matrix phase considering potential asymmetry in the tensile and compressive behavior. For such a reason, in the Tsai-Wu criterion it is assumed that $F_1 = F_2 = 0$, which means that the threshold for damage onset in the matrix phase is equal in tension and compression. In any case, the fact that compressive failure of fibers usually occurs at higher stress levels was included by not introducing any compressive damage of the fibers idealized phase. The arrows in the graphs indicate the path followed by matrix elements in the stress planes during linear simulations of T0, T30 and T45 that were performed with some simplified 2D models. It can be noticed that the strain softening is triggered at high values of shear stress with respect to the levels of normal stresses. The last parameter to be tuned for the strain softening regime was $p$, which was determined through a sensitivity analysis. To investigate this, strain softening was triggered in the matrix phase and $p$ was increased until a sharp stress decrease was obtained in matrix elements. Indeed, the parameter $p$ is important since it determines how fast the idealized fiber phase is overloaded when the matrix has reached the strain softening regime. Accordingly, it has a role in representing, at the high abstraction level involved in the macroscopic model developed in this work, how the tensile failure is activated by a critical accumulation of damage in the matrix, followed by pull-out and breakage of the fibers. Eventually, $p$ was set to 40.

Finally, the quasi-brittle law associated to the fibers idealized phase required the calibration of $\sigma^f_{di}$, $\sigma^f_{df}$ and $m$. The first two were statistically distributed in the volume of the material to simulate the presence of defects originated during the manufacturing process. Also in this case, a normal distribution was chosen, and it was required to calibrate a mean value and a standard deviation for $\sigma^f_{di}$ and $\sigma^f_{df}$. A sensitivity analysis driven by the flexural tests on *B0* specimens yielded to the values reported in Table 6.

The calibration and validation procedure is summarized in the workflow presented in Fig. 11.

#### 3.2.2. Correlation with tensile tests

Tensile simulations comprised all four lay-ups that were tested in the experimental campaign: *T0*, *T30*, *T45* and *TQI*. As explained in Appendix A1, the damage evolution law until strain softening was calibrated by using only *T45*, while the stress and strain at failure in *T0*, *T30*, and in *T45* were used to define the strain softening threshold. Hence, *T0*, *T30*, and *T45* validate the law in the phase of progressive damage

**Table 5**
Properties for the damage model.

| $a_1$ | $b_1$ | $c_1$ | $a_2$ | $b_2$ | $c_2$ |
|---|---|---|---|---|---|
| $1.34\ 10^{-2}$ | $-3.41\ 10^{-1}$ | $3.27\ 10^{-1}$ | $2.22\ 10^{-3}$ | $-3.64$ | $7.11\ 10^{-1}$ |

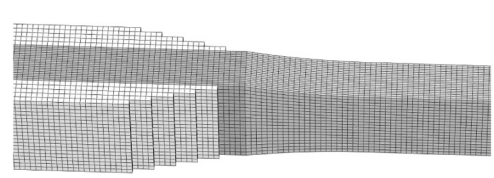

**Fig. 9.** Detail of the FE model of tensile specimens.

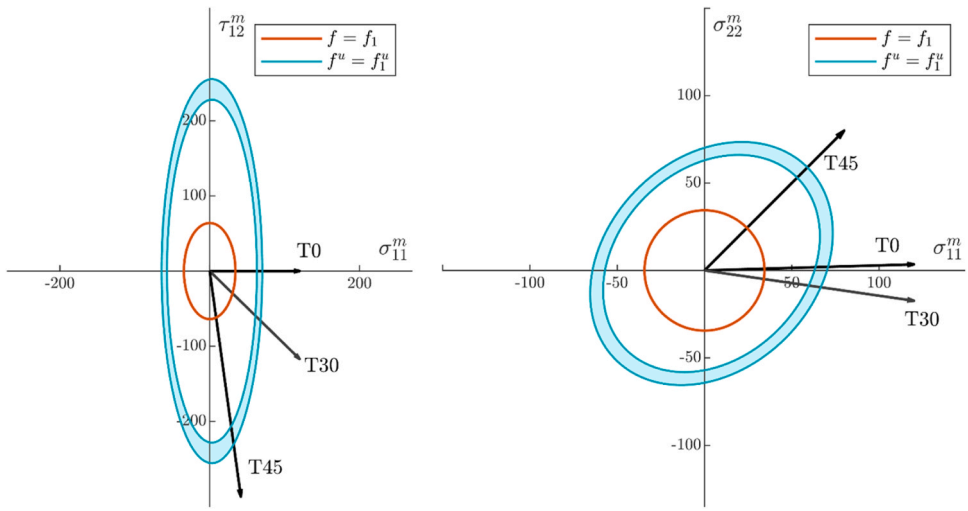


**Fig. 10.** Visual representation of the damage initiation function $f$ and of the strain softening onset function $f^u$.

**Table 6**
Identified parameters for the damage law of fibers.

| $m$ | Mean of $\sigma_{di}^f$ (MPa) | Mean of $\sigma_{df}^f$ (MPa) | STD of $\sigma_{di}^f$ and $\sigma_{df}^f$ (MPa) |
|---|---|---|---|
| 0.05 | 180 | 190 | 15 |

accumulation and *TQI* can be considered a validation for the whole calibrated model. The numerical engineering strain vs. stress curves measured along the loading direction are illustrated in Fig. 12-a. The numerical strain was computed through a virtual extensometer, which was set up between two preselected nodes within the gauge length. The last points of both the numerical and the experimental curves represented in the figure correspond to the load drop both in the FE analysis

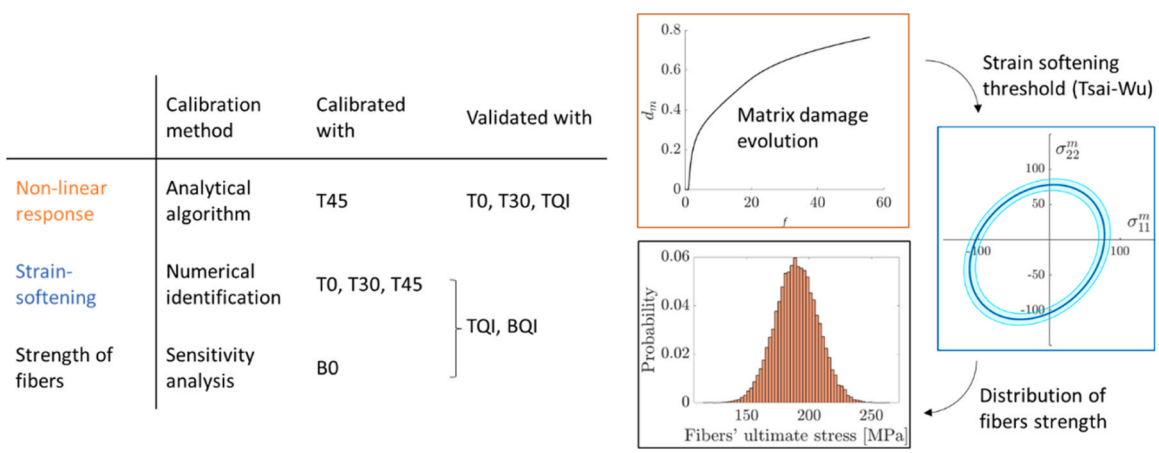


**Fig. 11.** Workflow of the identification and validation of the numerical model.

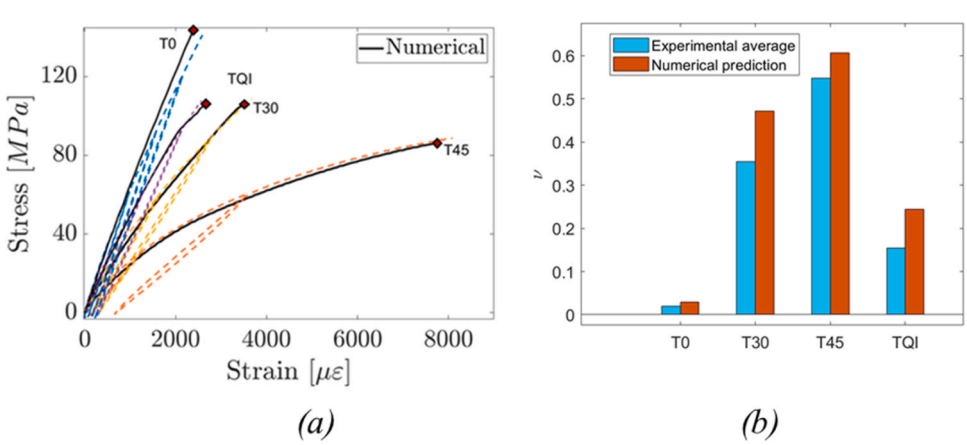


**Fig. 12.** (a) Stress vs. strain correlation in the direction of applied load and (b) prediction of Poisson's ratios.

and in the experiments and hence to the failure of specimens in the simulation and during the test, respectively. Additional virtual extensometers placed on the external surface of the specimens was used to investigate the transversal behavior of the model in the elastic range. Although the numerical Poisson's ratios exceed the experimental one, a good correlation was found, as depicted in Fig. 12-b. Numerical outcomes were almost in perfect agreement with the experiments in terms of ultimate loads, non-linearities and overall response. From a quantitative point of view, the material model is therefore extremely reliable.

Considering the mechanism that led to the failure of specimens in the FE simulations, it can be observed that for fiber dominated responses the achievement of a critical damage level in the matrix phase caused a localized stress decrease and an overloading of the fibers phase, as illustrated in Fig. 13. Eventually, this overloading caused the onset and rapid evolution of damage in the weakest fibers in the region of damaged matrix. For matrix dominated responses, especially for *T45* (see Fig. 13), neat cracks oriented as the reinforcement and almost undamaged fibers were recorded during simulations. For *TQI* and *T30* a mixed behavior was observed: in *TQI* the plies oriented at 45° were severely damaged and caused the failure also of the plies at 0°; in *T30* both fibers and matrix damaging were present and oriented along lines parallel to the reinforcement. The numerical damage mechanisms are thus considered coherent with the macroscopic ones that were highlighted in the experimental campaign, and the damage model based on the Tsai-Wu surfaces is capable of accounting for very different degrees of non-linearities and ultimate stresses and strains.

### 3.2.3. Correlation with bending tests and general considerations

Bending tests were also simulated in Abaqus/Explicit. Specimens were modelled by using the biphasic technique as in the case of tensile simulations, and rigid cylinders were used to introduce the load. The motion of the central loading cylinder was controlled by attributing a smoothly increasing velocity, and the interaction between cylinders and the specimen was modelled through a surface-to-surface contact [51]. The model size was reduced to approximately 140k elements by exploiting a symmetry along the width direction of specimens.

The numerical load vs. displacement curves were adequately correlated with the experimental outcomes both in terms of ultimate load and overall response (see Fig. 14). It should be remarked that the matrix damage in the compressed plies cannot be considered a reliable estimation, since it was not possible to obtain experimental evidence on the compressive behavior of the ceramic matrix.

For *BQI* simulations predicted ultimate loads that are in good agreement with tests characterized by values below the average, and the opposite occurred for *B0*. However, the material model was able to represent the bending to tensile strength ratio with acceptable approximation for both *B0/T0* and *BQI/TQI*. The capability of representing the bending to tensile strength ratio can be related to the interplay of two factors: (i) the through-the-thickness gradient of damage in the matrix, which mitigates the overloading of fibers when matrix reaches the strain softening threshold; and (ii) the statistical distribution of fiber strength, exploiting the fact that a smaller volume of material experiences high tensile stress concentrations during bending compared to tensile tests.

It is worth noting that, as in experiments, in bending simulations the final fracture propagated also in the upper side of the specimen (see Fig. 15), even though no compressive threshold was introduced for the onset of fiber damage. Fiber failure was always triggered by tensile stress: as soon as the lower tensed ply fails, stress transfers to the upper lamina that is then subjected to failure stress itself.

The developed material model allowed to produce tensile simulations where the final failure was dominated by the sharp stress decrease in the matrix phase during strain softening, and bending simulations where this effect was mitigated, thus increasing the strength of the specimens. The numerical failure mechanism can be conceptually considered in agreement with the material behavior, although, in the numerical analysis, the damage in the fibers evolved along a neat vertical straight line. Hence, the physical failure mechanism that is reported in Fig. 6(b) could not be represented in detail. Among other factors, such discrepancy can be attributed to the lack of representation of the out-of-plane failures. Despite the precautions taken in selecting the geometry of the specimens, it is possible that delamination could have been avoided by performing 4-point flexural tests. However, the overall ability of the simulations to catch the response of the material in bending can be deemed satisfactory.

The overall quality of the numerical predictions in terms of ultimate stress is summarized in Fig. 16. It can be observed that the predictions for *T0* and *B0* achieved an acceptable correlation with the experimental tests. However, they exceeded the average value, whereas an opposite trend occurred for the prediction of *BQI*. An explanation of this phenomenon may be related to the nature of the material, which is typically characterized by macroscopic defects with a characteristic length on the order of millimetres. These defects, which were not included in the models, likely had a more relevant effect in the case of very brittle behaviour, like in *T0* and *B0* case, rather than in specimens including off-axis plies, which are characterized by a more graceful and smoother failure mode. This consideration is supported by the considerably higher scattering observed in the *T0* tests with respect to the *T45* ones. An alternative interpretation suggests that the ply-by-ply models failed to capture the collaborative response between the matrix of ±45 and 0 plies during damaging. This may also explain the sudden deviation that characterizes the response of the *TQI* simulation before failure, which is caused by the damaging of the matrix in the ±45 laminae.

Eventually, to predict with good approximation the final failure of *T0* and *B0* without including any macroscopic defect in the highly refined mesh, it resulted necessary to reduce the average value of fibers strength, but this led to underestimate the experimental failure stress of *BQI*. However, all the predictions fall within the range of the experimental scattering, and most of them lie within the standard deviation evaluated after the experiments.

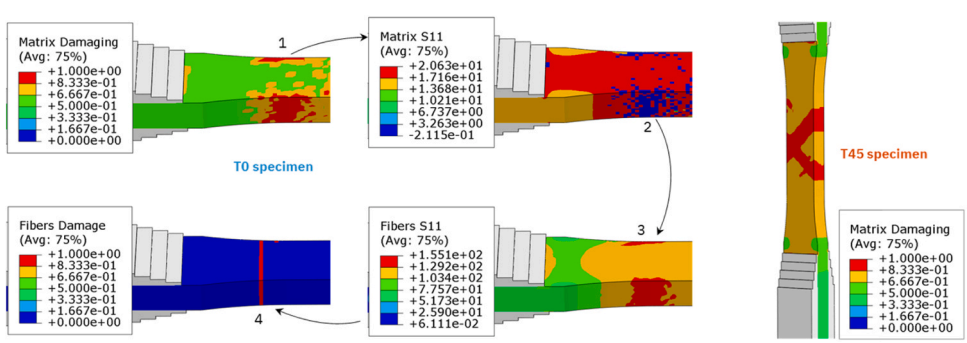


**Fig. 13.** Numerical failure mechanism for T0 and T45 specimens.

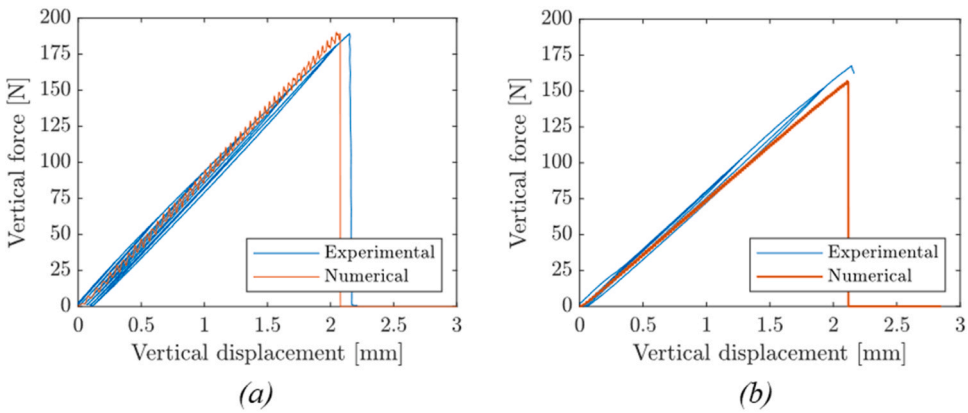


**Fig. 14.** Correlation of force vs. displacement curves (a) B0 (b) BQI.

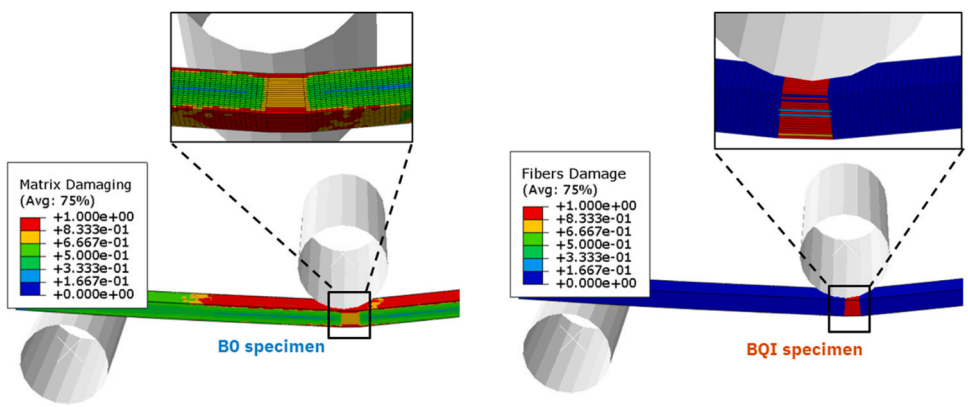


**Fig. 15.** Matrix damage in a B0 specimen (left) and fibers damage in a BQI specimen(right) after failure.

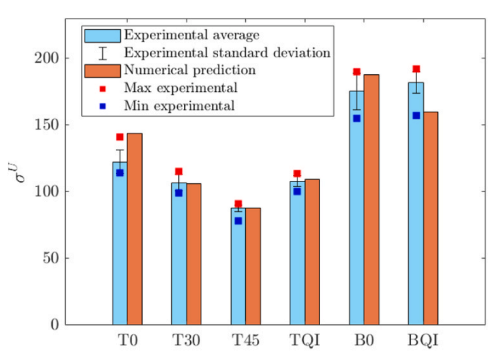


**Fig. 16.** Summary of the numerical predictions.

## 4. Conclusions

This work presented the development of a material model for LSI produced C/C-SiC laminates that achieved appreciable correlation with the response recorded during tensile and bending experiments. The decomposition of the composite material in two idealized and superimposed phases, which is a key aspect of the modelling technique, was found capable of separating matrix- and fibers- dominated responses during the simulations. The idealized phases were endowed with two separate damage models, whose aim was to represent at a higher level of abstraction the most significant complex mechanisms that occur at the microscale and involve the actual constituents of the material. The damage model attributed to the matrix phase was based on two Tsai-Wu surfaces that dictated the damage evolution and the strain-softening onset, which was found particularly suited to account for the response of different lay-ups, characterized by varying degrees of non-linearities and diverse stress/strains at failure.

The introduction of a statistical distribution for both the strength of the fibers and the threshold for strain softening in the matrix was fundamental to capture with good approximation the bending to tensile strength ratio that is typical of this family of materials. In addition, this helped to grasp within the numerical analyses the failure mechanism that several authors indicated to be responsible for the failure of C/C-SiC laminates, characterized by the key role attributed to the damage accumulated in the matrix, which triggers the final failure of the material.

In conclusion, the proposed material model and its calibration procedure are deemed to be an effective tool to investigate the response and support the design of CMC structural elements through FE analysis. Simulations were indeed able to represent the complex nonlinear response of all the lay-ups, to predict with good accuracy the ultimate loads, and to provide a reliable indication of the critical regions where failure should be expected, without any a-priori identification of the zones where the final fracture occurred.

## Funding

Funding was received for this work.

All of the sources of funding for the work described in this publication are acknowledged below:

*This work was supported by the Italian Space Agency (ASI) as part of the project AM3aC2A: Multi-scale approach for modelling CMC and UHTCMC materials.*

## CRediT authorship contribution statement

**Marco Riva:** Investigation, Methodology, Software, Visualization, Writing – original draft. **Lorenzo Cavalli:** Funding acquisition, Methodology, Resources, Supervision. **Antonio Maria Caporale:** Investigation, Validation, Writing – original draft. **Alessandro Airoldi:** Conceptualization, Funding acquisition, Project administration, Supervision, Writing – review & editing. **Edoardo Novembre:** Conceptualization, Investigation, Methodology, Software, Writing – original draft. **Mario De Stefano Fumo:** Funding acquisition, Supervision.

## Declaration of Competing Interest

No conflict of interest exists.

We wish to confirm that there are no known conflicts of interest associated with this publication and there has been no significant financial support for this work that could have influenced its outcome.

*Intellectual Property*

We confirm that we have given due consideration to the protection of intellectual property associated with this work and that there are no impediments to publication, including the timing of publication, with respect to intellectual property. In so doing we confirm that we have followed the regulations of our institutions concerning intellectual property.

*Authorship*

All listed authors meet the ICMJE criteria. We attest that all authors contributed significantly to the creation of this manuscript, each having fulfilled criteria as established by the ICMJE.

We confirm that the manuscript has been read and approved by all named authors.

We confirm that the order of authors listed in the manuscript has been approved by all named authors.

## Appendix A1. –Calibration of damage evolution law in the matrix

The algorithm relies on selecting the three points that define $f = 1, f = f_1$ and $f = f_2$ along the experimental $\sigma^{45}$-$\varepsilon^{45}$ curve of one representative *T45* test. Regarding the point $f = 1$, damage is equal to zero by definition. Within the context of the bi-phasic approach and under the reasonable assumption that fibers are undamaged until final failure, a value for $d_m$ can be univocally assigned to the points for which $f = f_1$ and $f = f_2$. These values can be obtained by enforcing in the two points the equivalence between the experimentally measured ($\overline{E_{11}^{45}}$) and the numerical secant modulus, which depends on the matrix damage variable $d_m$. The numerical secant modulus $E_{11}^{45}$ is expressed in Eq. A1 as a function of the stiffness matrix of the $\pm 45$ laminates $D_{ij}^{45}$. This procedure yields to the second order equation reported in Eq. A2 which, being damage intrinsically positive, admits only one solution.

$$E_{11}^{45} = D_{11}^{45}\left(1 - \frac{\left(D_{12}^{45}\right)^2}{D_{11}^{45}D_{22}^{45}}\right) \tag{A1}$$

$$\left(D_{11}^{45}f + (1-d_m)D_{11}^{45}m\right)\left(1 - \frac{\left(D_{12}^{45}f + (1-d_m)D_{12}^{45}m\right)^2}{\left(D_{11}^{45}f + (1-d_m)D_{11}^{45}m\right)\left(D_{22}^{45}f + (1-d_m)D_{22}^{45}m\right)}\right) = \overline{E_{11}^{45}} \tag{A2}$$

Once damages are computed, $f_1$ and $f_2$ can be evaluated by extrapolating the stress state in the selected points through the constitutive laws of the idealized phases. The other unknowns, which define the damage evolution before strain softening, are computed after formulating a linear system of equations (see Eq. A3) that conveniently enforces some conditions on the damage evolution.

$$\begin{bmatrix} 1 & 1 & 1 & 0 & 0 & 0 \\ 1 & f_1 & f_1^{-1} & 0 & 0 & 0 \\ 0 & 0 & 0 & 1 & f_1 & f_1^{-1} \\ 0 & 0 & 0 & 1 & f_2 & f_2^{-1} \\ 0 & -1 & f_1^{-2} & 0 & 1 & -f_1^{-2} \\ 0 & 0 & 0 & 0 & D_{12}^{45}mf_2 & -D_{12}^{m}f_2^{-1} \end{bmatrix} \begin{matrix} c_1 \\ \begin{bmatrix} a_1 \\ b_1 \\ c_2 \\ a_2 \end{bmatrix} \\ b_2 \end{matrix} = \begin{bmatrix} 0 \\ d_{m1} \\ d_{m1} \\ d_{m2} \\ 0 \\ D_{12}^{45}m(1-d_{m2}) - E^{\tan}/2 \end{bmatrix} \tag{A3}$$

The first four rows of Eq. A3 impose the exact value of damage at the switching points of the piecewise evolution function, the fifth one enforces the continuity of the derivative in the middle point, and the last one states approximately that the experimental ($E^{\tan}$) and the numerical tangential modulus in the point corresponding to ultimate load are equal. Assuming pure shear and that $\varepsilon_{12}$ is the only relevant in-plane strain component, the numerical tangential modulus can be approximated as $\partial\tau_{12}/\partial\varepsilon_{12}$. After performing the derivative, this condition reads as Eq. A4.

$$D_{12}^{45}m(1-d_{m2}) - \frac{E^{\tan}}{2} = \left(D_{12}^{45}mf_2\right)a_2 - \frac{D_{12}^{45}m}{f_2}b_2 \tag{A4}$$

## Appendix A2. – Identification of the strain-softening function for the matrix

Given the architecture of the reinforcement of the material, the strength in the two in-plane directions were set identical leading to the following identities: $S_{11}^{T} = S_{22}^{T} = S^{T}$ and $S_{11}^{C} = S_{22}^{C} = S^{C}$. Moreover, a mean value and a standard deviation were required to define the threshold value for the onset of strain-softening ($M$ and $D$, respectively). Assuming the classical fix $F_{12} = 1/2\sqrt{F_{11}F_{22}}$ and including the identities of Eq. 4 the strain softening

criterion was the one reported in Eq. A5.

$$\sqrt{\left(\frac{1}{S^T}-\frac{1}{S^C}\right)\tilde{\sigma}_{11}^m+\left(\frac{1}{S^T}-\frac{1}{S^C}\right)\tilde{\sigma}_{22}^m+\frac{\left(\tilde{\sigma}_{11}^m\right)^2}{S^TS^C}+\frac{\left(\tilde{\sigma}_{22}^m\right)^2}{S^TS^C}+\frac{\tilde{\sigma}_{11}^m\tilde{\sigma}_{22}^m}{S^TS^C}+\frac{\left(\tilde{\tau}_{12}^m\right)^2}{S_{12}^2}}=f_1^u(M,D) \tag{A5}$$

Employing a Monte Carlo like method for the identification of the parameters required the definition of a domain of interest. Its boundaries, which are reported in Table A 1, were set based on preliminary simulations where a tuning based on trial and error was performed. The resulting 5-dimensional space was sampled through a Latin Hypercube Sampling (LHS) to obtain 200 different observations. Each combination was used to set up the strain softening threshold in the material model, which was then implemented into the detailed model for the simulation of three types of tests: *T0*, *T30* and *T45*.

The performance of each observation was evaluated through an index function, written in Eq. A6, which computed the sum of the normalized distances between experimental and numerical failure points in the stress-strain plane calculated for each lay-up. The choice of this simple index function relied on the consideration that the onset of strain-softening mainly affected the final failure of specimens. The best performing solution, which led to the parameters of Table A 1, was taken as the identified strain softening threshold function for the material model.

$$I=\sum_{i=1}^{3}\left(\sqrt{\left(\frac{\sigma_i^{U,Exp}-\sigma_i^{U,Num}}{\sigma_i^{U,Exp}}\right)^2+\left(\frac{\varepsilon_i^{U,Exp}-\varepsilon_i^{U,Num}}{\varepsilon_i^{U,Exp}}\right)^2}\right) \tag{A6}$$

**Table A 1**
Properties for the strain-softening of the matrix phase.

| | Lower limit | Upper limit | Identified value |
|---|---|---|---|
| $S^T$ | 55 MPa | 65 MPa | 63 MPa |
| $S^C$ | 55 MPa | 200 MPa | 57 MPa |
| $S_{12}$ | 200 MPa | 250 MPa | 228 MPa |
| M | 0.8 | 1.2 | 1.06 |
| D | 0.05 | 0.3 | 0.06 |

## References


[1] N.P. Bansal, J. Lamon, American Ceramic Society, editors. Ceramic matrix composites: materials, modeling and technology, Wiley, Hoboken, NJ, 2015.
[2] B. Behrens, M. Müller, Technologies for thermal protection systems applied on re-usable launcher, Acta Astronaut. 55 (2004) 529–536, https://doi.org/10.1016/j.actaastro.2004.05.034.
[3] D.E. Glass, Ceramic Matrix Composite (CMC) Thermal Protection Systems (TPS) and Hot Structures for Hypersonic Vehicles. 15th AIAA international space planes and hypersonic systems and technologies conference, Dayton, Ohio, 2008, p. 2682.
[4] K.K. Chawla, Ceramic Matrix Composites. Composite Materials, Springer New York, New York, NY, 1987, pp. 134–149, https://doi.org/10.1007/978-1-4757-3912-1_7.
[5] W. Krenkel, B. Heidenreich, R. Renz, C/C-SiC Composites for Advanced Friction Systems, Adv. Eng. Mater. 4 (2002) 427–436, https://doi.org/10.1002/1527-2648(20020717)4:7<427::AID-ADEM427>3.0.CO;2-C.
[6] W. Krenkel, F. Berndt, C/C–SiC composites for space applications and advanced friction systems, Mater. Sci. Eng.: A 412 (2005) 177–181, https://doi.org/10.1016/j.msea.2005.08.204.
[7] P.J. Hofbauer, F. Raether, E. Rädlein, Finite element modeling of reactive liquid silicon infiltration, J. Eur. Ceram. Soc. 40 (2020) 251–258, https://doi.org/10.1016/j.jeurceramsoc.2019.09.041.
[8] W. Krenkel, Cost Effective Processing of Cmc Composites by Melt Infiltration (Lsi-Process), in: M. Singh, T. Jessen (Eds.), Ceramic Engineering and Science Proceedings, vol. 22, John Wiley & Sons, Inc., Hoboken, NJ, USA, 2001, pp. 443–454, https://doi.org/10.1002/9780470294680.ch52.
[9] M. Patel, K. Saurabh, V.V.B. Prasad, J. Subrahmanyam, High temperature C/C–SiC composite by liquid silicon infiltration: a literature review, Bull. Mater. Sci. 35 (2012) 63–73, https://doi.org/10.1007/s12034-011-0247-5.
[10] M.H. Hon, R.F. Davis, Self-diffusion of14C in polycrystalline β-SiC, J. Mater. Sci. 14 (1979) 2411–2421, https://doi.org/10.1007/BF00737031.
[11] F.H. Gern, R. Kochendörfer, Liquid silicon infiltration: description of infiltration dynamics and silicon carbide formation, Compos. Part A: Appl. Sci. Manuf. 28 (1997) 355–364, https://doi.org/10.1016/S1359-835X(96)00135-2.
[12] X. Peng, L. Zhuan, Z. Zi-bing, X. Xiang, The morphology and mechanism of formation of SiC in C/C-SiC composites fabricated by liquid silicon infiltration, J. Ceram. Process. Res. (2010).
[13] W. Krenkel, C/C-Sic Composites for Hot Structures and Advanced Friction Systems, in: W.M. Kriven, H.-T. Lin (Eds.), Ceramic Engineering and Science Proceedings, vol. 24, John Wiley & Sons, Inc., Hoboken, NJ, USA, 2003, pp. 583–592, https://doi.org/10.1002/9780470294826.ch85.
[14] B. Heidenreich, W. Krenkel, B. Lexow, Development of Cmc-Materials for Lightweight Armor, in: W.M. Kriven, H.-T. Lin (Eds.), Ceramic Engineering and Science Proceedings, vol. 24, John Wiley & Sons, Inc., Hoboken, NJ, USA, 2003, pp. 375–381, https://doi.org/10.1002/9780470294802.ch55.
[15] K. Tushtev, J. Horvath, D. Koch, G. Grathwohl, Deformation and Failure Modeling of Fiber Reinforced Ceramics with Porous Matrix, Adv. Eng. Mater. 6 (2004) 664–669, https://doi.org/10.1002/adem.200400094.
[16] M. Genet, L. Marcin, E. Baranger, C. Cluzel, P. Ladevèze, A. Mouret, Computational prediction of the lifetime of self-healing CMC structures, Compos. Part A: Appl. Sci. Manuf. 43 (2012) 294–303, https://doi.org/10.1016/j.compositesa.2011.11.004.
[17] U. Santhosh, J. Ahmad, G. Ojard, R. Miller, Y. Gowayed, Deformation and damage modeling of ceramic matrix composites under multiaxial stresses, Compos. Part B: Eng. 90 (2016) 97–106, https://doi.org/10.1016/j.compositesb.2015.12.017.
[18] D. Zhang, P. Meyer, A.M. Waas, An experimentally validated computational model for progressive damage analysis of notched oxide/oxide woven ceramic matrix composites, Compos. Struct. 161 (2017) 264–274, https://doi.org/10.1016/j.compstruct.2016.11.001.
[19] G. Zhao, J. Tang, J. Wang, Y. Chen, Y. Feng, Y. Chen, et al., An Advanced Finite Element Modeling for the Failure of Notched Ceramic Matrix Composite With TFP Patch Reinforcement, Front. Mater. 8 (2021) 701193, https://doi.org/10.3389/fmats.2021.701193.
[20] S. Hofmann, B. Öztürk, D. Koch, H. Voggenreiter, Experimental and numerical evaluation of bending and tensile behaviour of carbon-fibre reinforced SiC, Compos. Part A: Appl. Sci. Manuf. 43 (2012) 1877–1885, https://doi.org/10.1016/j.compositesa.2012.07.017.
[21] S. Hofmann, D. Koch, Predicting the mechanical behaviour of carbon fibre reinforced silicon carbide with interlaminar manufacturing defects, MATEC Web Conf. 29 (2015) 00012, https://doi.org/10.1051/matecconf/20152900012.
[22] S. Hofmann, Mode I delamination onset in carbon fibre reinforced SiC: Double cantilever beam testing and cohesive zone modelling, Eng. Fract. Mech. 182 (2017) 506–520, https://doi.org/10.1016/j.engfracmech.2017.05.018.
[23] B.N. Cox, W.C. Carter, N.A. Fleck, A binary model of textile composites—I. Formulation, Acta Metall. Et. Mater. 42 (1994) 3463–3479, https://doi.org/10.1016/0956-7151(94)90479-0.
[24] J. Xu, B.N. Cox, M.A. McGlockton, W.C. Carter, A binary model of textile composites—II. The elastic regime, Acta Metall. Et. Mater. 43 (1995) 3511–3524, https://doi.org/10.1016/0956-7151(95)00057-3.
[25] M.A. McGlockton, B.N. Cox, R.M. McMeeking, A Binary Model of textile composites: III high failure strain and work of fracture in 3D weaves, J. Mech. Phys. Solids 51 (2003) 1573–1600, https://doi.org/10.1016/S0022-5096(03)00038-3.

[26] Q.D. Yang, K.L. Rugg, B.N. Cox, D.B. Marshall, Evaluation of Macroscopic and Local Strains in a Three-Dimensional Woven C/SiC Composite, J. Am. Ceram. Soc. 88 (2005) 719–725, https://doi.org/10.1111/j.1551-2916.2005.00156.x.
[27] S. Flores, A.G. Evans, F.W. Zok, M. Genet, B. Cox, D. Marshall, et al., Treating matrix nonlinearity in the binary model formulation for 3D ceramic composite structures, Compos. Part A: Appl. Sci. Manuf. 41 (2010) 222–229, https://doi.org/10.1016/j.compositesa.2009.10.020.
[28] J. Jung, S.L. Dos Santos E Lucato, A CDM-BASED BINARY MODEL FOR THE PROGRESSIVE DAMAGE PREDICTION OF SiC/SiC CERAMIC MATRIX COMPOSITES UNDER TENSION LOADING, Int. J. Multiscale Comput. Eng. 19 (2021) 1–15, https://doi.org/10.1615/IntJMultCompEng.2021040257.
[29] G. Jefferson, C. Przybyla, L. Zawada, PREFACE: ASSESSMENT OF DAMAGE PROGRESSION MODELS FOR SiC/SiC CERAMIC MATRIX COMPOSITES, Int. J. Multiscale Comput. Eng. 19 (2021) v–xiv, https://doi.org/10.1615/IntJMultCompEng.2021041807.
[30] G. Camus, Development of damage in a 2D woven C/SiC composite under mechanical loading: I. Mechanical characterization, Compos. Sci. Technol. 56 (1996) 1363–1372, https://doi.org/10.1016/S0266-3538(96)00094-2.
[31] F. Breede, D. Koch, E. Maillet, G.N. Morscher, Modal acoustic emission of damage accumulation in C/C–SiC composites with different fiber architectures, Ceram. Int. 41 (2015) 12087–12098, https://doi.org/10.1016/j.ceramint.2015.06.026.
[32] S. Flauder, N. Langhof, W. Krenkel, S. Schafföner, Size effect of carbon fiber-reinforced silicon carbide composites (C/C-SiC): Part 1 – bending load and statistical effects, J. Eur. Ceram. Soc. 41 (2021) 6805–6814, https://doi.org/10.1016/j.jeurceramsoc.2021.07.040.
[33] A. Airoldi, C. Mirani, L. Principito, A bi-phasic modelling approach for interlaminar and intralaminar damage in the matrix of composite laminates, Compos. Struct. 234 (2020) 111747, https://doi.org/10.1016/j.compstruct.2019.111747.
[34] M. Riva, A. Airoldi, A. Maria Caporale, L. Cavalli, M. De Stefano Fumo, Interlaminar Response of LSI-Produced C/SiC Ceramic Matrix Composites: Experiments and Modelling, Compos. Part A: Appl. Sci. Manuf. (2023) 107774, https://doi.org/10.1016/j.compositesa.2023.107774.
[35] C28 Committee. Test Method for Monotonic Tensile Behavior of Continuous Fiber-Reinforced Advanced Ceramics with Solid Rectangular Cross-Section Test Specimens at Ambient Temperature. ASTM International; n.d. https://doi.org/10.1520/C1275-15.
[36] S. Flauder, I. Bombarda, R. D'Ambrosio, N. Langhof, A. Lazzeri, W. Krenkel, et al., Size effect of carbon fiber-reinforced silicon carbide composites (C/C-SiC): Part 2 - tensile testing with alignment device, J. Eur. Ceram. Soc. 42 (2022) 1227–1237, https://doi.org/10.1016/j.jeurceramsoc.2021.11.044.
[37] C28 Committee. Test Method for Flexural Properties of Continuous Fiber-Reinforced Advanced Ceramic Composites. ASTM International; n.d. https://doi.org/10.1520/C1341-13R18.
[38] Munalli D., Dimitrakis G., Chronopoulos D., Greedy S., Long A. The use of free-space microwave non-destructive techniques: simulation of damage detection in carbon fibre reinforced composites. 11th Symposium on NDT in Aerospace, PARIS-SACLAY: 2019.
[39] C. Tang, A. Dang, T. Li, T. Zhao, H. Li, S. Jiao, Influence of fiber content on C/C-SiC brake materials fabricated by compression molding and hot sintering, Tribology Int. 136 (2019) 404–411, https://doi.org/10.1016/j.triboint.2019.04.009.
[40] D.B. Marshall, A.G. Evans, Failure Mechanisms in Ceramic-Fiber/Ceramic-Matrix Composites. J. Am. Ceram. Soc. 68 (1985) 225–231, https://doi.org/10.1111/j.1151-2916.1985.tb15313.x.
[41] F. Hild, J.-M. Domergue, F.A. Leckie, A.G. Evans, Tensile and flexural ultimate strength of fiber-reinforced ceramic-matrix composites, Int. J. Solids Struct. 31 (1994) 1035–1045, https://doi.org/10.1016/0020-7683(94)90010-8.
[42] A. Airoldi, E. Novembre, C. Mirani, G. Gianotti, R. Passoni, C. Cantoni, A model for damage and failure of carbon-carbon composites: development and identification through Gaussian process regression, Mater. Today Commun. 35 (2023) 106059, https://doi.org/10.1016/j.mtcomm.2023.106059.
[43] Airoldi A., Baldi A., Mostosi V., Sala G. A BI-PHASIC APPROACH TO MODEL PROGRESSIVE MATRIX DAMAGE IN COMPOSITES: DEVELOPMENT AND APPLICATION 2012.
[44] D. Coutellier, P. Rozycki, Multi-layered multi-material finite element for crashworthiness studies, Compos. Part A: Appl. Sci. Manuf. 31 (2000) 841–851, https://doi.org/10.1016/S1359-835X(00)00022-1.
[45] R.M. Jones. Mechanics of Composite Materials, 2nd ed, CRC Press, 2018, https://doi.org/10.1201/9781498711067.
[46] S.W. Tsai, E.M. Wu, A General Theory of Strength for Anisotropic Materials, J. Compos. Mater. 5 (1971) 58–80, https://doi.org/10.1177/002199837100500106.
[47] Y. Shi, N. Jain, D. Koch, Investigation and modeling of tensile failure properties of wound ceramic matrix composites, Compos. Part A: Appl. Sci. Manuf. 114 (2018) 316–326, https://doi.org/10.1016/j.compositesa.2018.08.029.
[48] M. Ferraiuolo, R. Scigliano, A. Riccio, E. Bottone, M. Rennella, Thermo-structural design of a Ceramic Matrix Composite wing leading edge for a re-entry vehicle, Compos. Struct. 207 (2019) 264–272, https://doi.org/10.1016/j.compstruct.2018.09.024.
[49] N. Jain, D. Koch, Prediction of Failure in Ceramic Matrix Composites Using Damage-Based Failure Criterion, J. Compos Sci. 4 (2020) 183, https://doi.org/10.3390/jcs4040183.
[50] J. Li, G. Jiao, B. Wang, L. Li, C. Yang, Damage characteristics and constitutive modeling of the 2D C/SiC composite: Part II – Material model and numerical implementation, Chin. J. Aeronaut. 28 (2015) 314–326, https://doi.org/10.1016/j.cja.2014.10.027.
[51] Dassault Systèmes Simulia. ABAQUS/Standard User's Manual, Version 6.14. Dassault Systèmes Simulia Corp.; 2014.
[52] B. Basu, D. Tiwari, D. Kundu, R. Prasad, Is Weibull distribution the most appropriate statistical strength distribution for brittle materials? Ceram. Int. 35 (2009) 237–246, https://doi.org/10.1016/j.ceramint.2007.10.003.